NANOSYSTEMS:
PHYSICS, CHEMISTRY, MATHEMATICS

Vorotnikov V.A., et al. *Nanosystems: Phys. Chem. Math.*, 2024, **15** (1), 65–79.
http://nanojournal.ifmo.ru
DOI 10.17586/2220-8054-2024-15-1-65-79

Original article

Equilibrium of intrinsic and impurity point defects in Ca-doped $Sm_2Zr_2O_7$

Vladimir A. Vorotnikov[1,2], Semyon A. Belyakov[3], Alexey V. Ivanov[1,2], Yulia V. Novikova[3], Anna Yu. Stroeva[1], Vadim V. Grebenev[4], Dmitry N. Khmelenin[4], Olga V. Emelyanova[4], Maksim S. Plekhanov[5], Anton V. Kuzmin[1,2]

[1]Institute of Chemistry and Ecology, Vyatka State University, Kirov, Russia

[2]Institute of Solid-State Chemistry and Mechanochemistry SB RAS, Novosibirsk, Russia

[3]Institute of High-Temperature Electrochemistry UB RAS, Yekaterinburg, Russia

[4]Shubnikov Institute of Crystallography of Federal Scientific Research Centre "Crystallography and Photonics" of the RAS, Moscow, Russia

[5]Institute of Crystallography, RWTH Aachen University, Aachen, Germany

Corresponding author: Anton V. Kuzmin, a.v.kuzmin@yandex.ru

PACS 82.45.Gj, 82.33.Pt

ABSTRACT In this work, a doping strategy was used to achieve a good conductivity in samarium zirconate which crystallizes in the pyrochlore. The production of nanopowders made it possible to form high-density ceramics with an optimal microstructure. It is shown that intrinsic and impurity defects coexist in $Sm_{2-x}Ca_xZr_2O_{7-\delta}$, impairing ion transport at high doping levels. Despite this, $Sm_{1.95}Ca_{0.05}Zr_2O_{7-\delta}$ maintains low activation energy of the parent and has good ionic conductivity (10^{-3} S·cm^{-1} at 600 °C) which is one of the largest among oxide pyrochlores. It has been shown to have a good chemical stability. The material has a thermal expansion coefficient (TEC) of 12 ppm K^{-1} which is higher than YSZ and provides better compatibility with electrode materials. The above makes it possible to successfully use it as a highly stable oxygen electrolyte or an intermediate thin layer at the electrolyte-electrode interface in electrochemical devices.

KEYWORDS solid oxide electrolyte, pyrochlores, grain boundary conductivity, nanoscale powders, combustion method

ACKNOWLEDGEMENTS The research was partially supported by the Russian Science Foundation (Grant No. 22-23-01121).

FOR CITATION Vorotnikov V.A., Belyakov S.A., Ivanov A.V., Novikova Yu.V., Stroeva A.Yu., Grebenev V.V., Khmelenin D.N., Emelyanova O.V., Plekhanov M.S., Kuzmin A.V. Equilibrium of intrinsic and impurity point defects in Ca-doped $Sm_2Zr_2O_7$. *Nanosystems: Phys. Chem. Math.*, 2024, **15** (1), 65–79.

1. Introduction

In recent years, high thermal, chemical and radiation stability has led to great interest in lanthanide zirconates $Ln_2Zr_2O_7$ with a pyrochlore structure. Due to their good thermomechanical characteristics, compositions such as $Gd_2Zr_2O_7$, and $(La_{1-x}Gd_x)_2Zr_2O_7$ are recommended as thermal barrier coating materials [1–6], which is one of the promising applications of pyrochlores. Having high chemical stability, pyrochlores are used as electrolytes for oxygen sensors for aggressive environments, such as Li-based melts [7–9]. High radiation resistance allows pyrochlores to be used as materials for the encapsulation of nuclear waste [10, 11]. Pyrochlores are also considered as promising oxygen-ion conductors for solid oxide fuel cells (SOFCs), so a large amount of work is aimed at studying the relationship between structure and transport properties [12–14].

The mechanism of disorder in pyrochlores is based on its own oxygen deficiency. Partially disordered pyrochlore phases are better ionic conductors than highly disordered fluorite materials of the same composition due to lower activation energies (E_A) for the migration of oxygen ions. For example, E_A is significantly lower in the pyrochlore-type defective gadolinium zirconate $Gd_2Zr_2O_7$ than in its fluorite-type analogue [15]. The pyrochlore crystal structure can be derived from the fluorite structure by doubling the unit cell, removing one out of every eight anions, and placing the cations and anions at four crystallographically nonequivalent positions. Using the setup of Tabira et al. [16], the A cation is in the 8-coordinated 16c positions and the B cation is in the 6-coordinated 16d positions (Wyckoff notation). The anions are distributed between two 4-coordinated positions O(48f) and O(8b). One 4-coordinate position O(8b) is free. A decrease in the lanthanide radius in $Ln_2Zr_2O_7$ leads to a gradual occupation of this position [17–19].

Previously, using atomistic modeling, it was proposed that the most stable intrinsic defect in pyrochlores is the oxygen Frenkel pair, consisting of a vacant O(48f) site and an interstitial ion located at the O(8a) position, and that the diffusion of

oxygen ions occurs due to hopping between O(48f) sites [20–24]. Thus, the oxygen conductivity in disordered pyrochlores depends significantly on the energy of formation of this type of defect. The presence of disorder in the cationic sublattice leads to a decrease in this energy value, since cationic disorder increases the similarity between nonequivalent oxygen sites and thereby contributes to the formation of defects in the oxygen sublattice [21, 24–28].

Among the zirconate pyrochlore series, $Gd_2Zr_2O_7$ has the greatest internal disorder [29], demonstrating high conductivity values of about 0.01 S·cm^{-1} at fairly high temperatures $\sim$ 900 °C [30–34]. However, the most disordered pyrochlores are not necessarily the best conductors of oxygen ions and exhibit systematically higher E_A for oxygen ion migration. Due to the increase in E_A, the conductivity at lower temperatures drops significantly. Thus, the highest conductivity values are usually achieved in partially disordered pyrochlores. This statement can be traced using the example of isovalent doping, when disorder is regulated by varying the ratio of the ionic radii of A and B cations. Doping Gd in $Gd_{2-x}M_xZr_2O_7$ with larger La or Nd leads to a decrease in the E_A and the peak conductivity value reaches $Gd_{1.7}La_{0.3}Zr_2O_7$ and equimolar $GdNdZr_2O_7$, respectively [30, 31]. In $Gd_2Sn_{2-x}Zr_xO_7$, the conductivity increases with the concentration of Zr which is slightly larger than Sn although the E_A changes slightly [32]. For $Gd_2Zr_{2-x}Ti_xO_7$ pyrochlores, a decrease in the E_A is observed with increasing content of smaller Ti as the structure becomes more ordered [33]. A decrease in the average size of cations in the A-position, the replacement of Gd by smaller lanthanides such as Dy, Y or Er, increases the intrinsic structural disorder of $Gd_2Zr_2O_7$ and induces the pyrochlore-fluorite phase transition [34]. In this case, the replacement of Gd with larger cations, such as Sm, Nd or La, orders the pyrochlore structure.

Heterovalent acceptor-type doping is a strategy to significantly increase oxygen deficiency, as well as cationic disorder. Those dopants that cause the least deformation of the crystal lattice of the base material have the lowest dissolution energy and give the highest conductivity of materials, therefore the replacement of lanthanides with Ca in $Ln_2Zr_2O_7$ pyrochlores is usually most advantageous [21, 23, 35]. Against the background of the fairly well-studied mechanism of acceptor doping in both ordered $La_2Zr_2O_7$ [23, 36–43] and noticeably disordered $Gd_2Zr_2O_7$ [7–9, 44–46, 48], moderately disordered $Sm_2Zr_2O_7$ has been less studied, although it should combine the advantages of the previous two. Liu et al. [49–51] even made attempts to take advantage of equimolar $GdSm_{1-x}M_xZr_2O_{7-\delta}$ (M = Ca, Mg) compositions. Without the dopant, the conductivity reaches 0.001 S·cm^{-1} at 600 °C, but decreases for both dopants due to the increasing E_A. Sm and Ca have very similar ionic radii [52]. Despite this, it was reported that the solubility of Ca in $Sm_2Zr_2O_7$ is low [46, 53], although the mentioned authors used a solid-phase synthesis method. The conductivity of the materials at 600 °C is about $4{\cdot}10^{-4}$ S·cm^{-1} and decreases slightly with increasing concentration of Ca dopant, and E_A also increase. Our study reveals a noticeable increase in conductivity at low (2.5 at. %) Ca dopant concentrations in $Sm_{2-x}Ca_xZr_2O_{7-\delta}$ without a significant effect on the E_A.

The microstructure of the samples also affects the level of conductivity; the electrolyte materials must be of high density and approximately equal grain sizes so that the processes occurring in the bulk and at the grain boundary are more understandable. For example, in [46], $Sm_{2-x}Ca_xZr_2O_{7-\delta}$ ceramics obtained by mechanical activation have a relative density of 89 – 92.6 % and a strong variation in grain sizes from 100-300 nm to several microns is recorded. In work [47], we synthesized the proton conductor $La_{1-x}Sr_xScO_{3-\delta}$ by the following methods: solid state reaction, combustion and co-deposition. It has been shown that only the combustion method leads to the production of highly dispersed powders with particle sizes up to 100 nm. As a result, this method proved to be the most effective in obtaining a given microstructure of ceramic samples. Hence, a high density relative to the theoretical one (> 95 %) and a uniform size distribution of ceramic grains have been achieved. The influence of the defect formation model and grain boundary effects on the conductivity of materials is also discussed in detail. This work is devoted to the synthesis of nanostructured samarium zirconate powders, the production of dense ceramics and the study of its physico-chemical properties.

2. Experimental

2.1. Sample preparation

The citrate-nitrate combustion technique was used for the preparation of $Sm_{2-x}Ca_xZr_2O_{7-\delta}$ (where $x = 0$; 0.05; 0.075; 0.01; 0.125 and 0.15, then SZ; SCZ5, SCZ7.5, SCZ10, SCZ12.5 SCZ15, total – SCZ) samples. Samarium oxide Sm_2O_3, calcium carbonate $CaCO_3$ and zirconium oxynitrate $ZrO(NO_3)_2$, all high purity reagents, were used as precursors. To achieve high homogenization of oxide-forming cations, a solution mixing stage was carried out. For this purpose, a solution of $ZrO(NO_3)_2$ with the precise concentration was prepared. The calculated Sm_2O_3 weights, taking into account the mass loss coefficient during calcination and the drained $CaCO_3$ in a proportional amount of CaO, were transferred to a nitrate solution when interacting with nitric acid (high purity reagent) and an aliquot of zirconium oxynitrate solution was added. Further, citric acid (high purity reagent) was added to the solution in a ratio of 3/1 to the mass of the resulting oxide and evaporated at a temperature of 130 °C until the combustion reaction took place. The obtained powders were annealed at a temperature of 800 °C (1 hours) to remove the organic residues and carbon black. After this, additional homogenization of the powdered mixture was carried out in an isopropyl alcohol medium using a PM 100 (Retch GmbH, Haan, Germany) planetary ball mill for 1 hour (350 rpm). The dried powders of all compositions

were subjected to preliminary synthesis at a temperature of 1100 °C for 2 hours. After that, the samples were formed by isostatic pressing at 600 MPa and then sintered in air at 1600 °C for 5 hours in a backfill of the appropriate composition.

2.2. Exposure to various atmospheres

The humidity of gas passing through the samples was set using a thermostated vessel with water of a room temperature. The dry atmosphere was reached by a gas passage through synthetic zeolites.

The samples were calcined before analyzes at 1000 °C for 20 hours when blown with dry air, and also at 600 °C without holding when blown in laboratory air. The stability to reduction was checked by holding samples at 850 °C for 250 hours in a flow of dry hydrogen.

2.3. X-ray diffraction

The phase composition of the samples was characterized by a X-ray diffractometer TDM-20 (Tongda, Hong Kong, China) with Cu Kα ($\lambda = 1.5418$ Å) radiation with step scan 0.0095° (2θ = 12 – 135°, exposure 1.3 s). The cubic lattice parameters were refined from XRD patterns by Le Bail method. The initial symmetry group and lattice parameters were taken for $Sm_2Zr_2O_7$ (ICSD 261415).

2.4. Electron microscopy

The surface morphology and cross section of the ceramics were studied by scanning electron microscopy (SEM). The cross sections were performed by grinding and polishing samples with water-based diamond abrasives. SEM images of the cross sections were obtained on a microscope JSM-6510 LV (JEOL, Tokyo, Japan), and the elemental distribution was studied by energy-dispersive X-ray (EDX) spectroscopy using an Inca X-MAX spectrometer system (Oxford Instruments, Abingdon, UK).

In order to investigate microstructure and elemental content of selected samples at subgrain scale, transmission electron microscopy (TEM) study was carried out using OSIRIS TEM (Thermo Fisher Scientific, Waltham, USA) equipped by high-angle annular dark-field (HAADF) detector (Fischione, Corporate Circle, Export, USA) and energy-dispersive spectrometer Super-X EDXS (Bruker, Billerica, USA). TEM data processing was performed in Digital Micrograph 3.4 (Gatan Inc., Pleasanton, USA) and Esprit (Bruker, Billerica, USA) software. The cross-sectional TEM samples were prepared by means of focused ion beam FIB lift-out technique using Scios Dual Beam (Thermo Fisher Scientific, Waltham, USA).

2.5. Dilatometry

Measurements of the thermal expansion were carried out in a quartz cell using the Tesatronic TT-80 (TESA, Renens, Switzerland) meter with a high-precision measuring probe GT 21HP (TESA, Renens, Switzerland). Before the experiment, the cell was calibrated to deduct the contribution of quartz's own expansion. Thermal expansion measurements were implemented during heating/cooling (speed 120 °C/hour) in the temperature range of 50 – 900 °C in moist (pH_2O = 2.8 kPa) and dry ($pH_2O < 0.1$ kPa) air. Thermal expansion coefficients (TEC) were calculated from the linear sections of the $\Delta L/L_0 - T$ dependencies. Humidity induced chemical expansion was measured during the transition from dry atmosphere ($pH_2O < 0.1$ kPa) to humidified atmospheres (pH_2O = 0.6 and 2.8 kPa) at isothermal exposure ($T = 600$ °C).

2.6. DC and AC conductivity

The total electrical conductivity of ceramic samples was measured by a four-probe DC method using a RM3545-02 (Hioki, Nagano, Japan) ohmmeter. The prepared samples had the geometry of rectangular bars with dimensions of about $12 \times 3 \times 3$ mm. Pt paste and wires were used as electrodes, which was baked to the faces of the samples at a temperature of 1100 °C during 1 hour. The measurements were carried out in the temperature range of 400 – 900 °C in heating/cooling modes in increments of 20 °C. An isothermal exposure at each temperature until the equilibrium resistance values were reached.

The electrochemical impedance spectroscopy (EIS) was applied in a two-probe mode. The samples were tablets with a diameter of 10 mm and a thickness of 1 mm. Ag paste was applied by painting in the form of a 5 by 5 mm area and baked at 800 °C for 2 hours. In order to reduce the polarization resistance of the electrodes, they were impregnated with a solution of cerium and terbium nitrates and slowly heated to 800 °C at a rate of 20 °C/hour, according to the method of [54]. The measurements were implemented on a SP-200 (Bio-Logic, Seyssinet-Pariset, France) equipment in the temperature range 300 – 400 °C with the step of 25 °C, and in the frequency range 3 MHz – 0.1 Hz at an AC voltage amplitude of 100 mV. The distribution of relaxation times (DRT) technique was employed for the analysis of the spectra [55]. The Tikhonov regularization method was applied [56]. The accuracy of the selection of the regularization coefficient was based on a comparison of the DRT functions of the experimental spectrum and the simulated DRT spectrum from the equivalent circuit [57].

3. Results and discussion

3.1. Crystal structure and morphology

Figure A1 shows typical XRD patterns for SCZ samples. Fig. 1 shows the values of unit cell parameters for samples of two series, as well as literature data. Samples of the first series were calcined in dry air at 1000 °C for 20 hours. Samples of the second series were calcined in laboratory air at 600 °C without holding. One can see a noticeable scatter of parameters for the two series, as well as for the literature data. Thus, heat treatment conditions affect the value of the unit cell parameter. It is known that the formation of the pyrochlore phase passes through the fluorite phase, therefore the unit cell parameter depends on the annealing temperature [58]. First, the synthesis method influences. In all the cited literature references, except for [59], the materials were obtained by the solid-phase synthesis method. Further, the maximum annealing temperature, cooling rate and atmosphere influence. One can compare the annealing conditions using the example of SZ material: in [60], double calcination was used at 1400 °C for 10 hours; in [61], samples were sintered at 1400 – 1600 °C for 8 hours; in [53], there was annealing at 1700 °C for 10 hours; and in [46], there was annealing at 1600 °C for 4 – 10 hours. In [59], a solution citrate synthesis method was used with final calcination only at 800 °C, although one should expect a much higher combustion temperature for a mixture of citrates and ethylene glycol.

In this work, we chose the method of slow combustion (about 12 hours at a temperature of 130 °C) with the addition of three times the amount of citric acid in relation to the mass of the resulting oxide. This method allows us to obtain powders having the specific surface area of after annealing at 800 °C amounted to 80.000 – 85.000 cm^2/cm^3 which defines their nano-dimensional character even at this stage of synthesis. At the same time, the powders have already been heat treated, which inevitably led to particle agglomeration. It should be borne in mind that the granulometric composition of powders without heat treatment does not make sense to evaluate due to the presence of additional components, organic residues, and/or the presence of an oxide-forming mixture still in the salt state. The obtained highly dispersed powders led to the production of high-density ceramics (more than 95 % relative to the theoretical one) with a uniform grain size distribution. The final sintering was implemented at 1600 °C for 5 hours. Synthesis and heat treatment conditions primarily affect the concentration of antistructural defects such as Zr in the Sm sublattice and, conversely, Sm in the Zr sublattice [24, 26, 27]. This can also affect the distribution of the dopant over both sublattices.

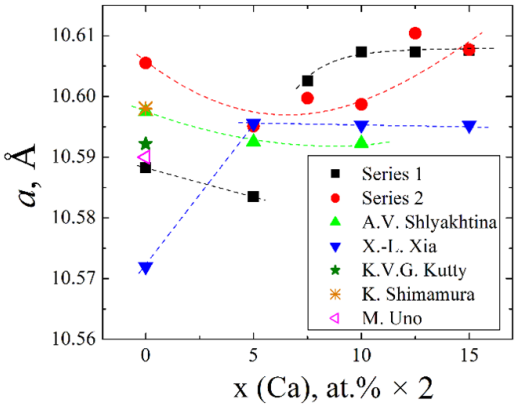

FIG. 1. Cubic unit cell parameter of SCZ as a function of dopant concentration. Series 1 means samples pre-calcined at 1000 °C for 20 hours in dry air, Series 2 means samples pre-calcined at 600 °C in laboratory air without holding. Literature results from papers by Shlyakhtina et al. [46], Xia et al. [53], Govindan Kutty et al. [60], Shimamura et al. [61] and Uno et al. [59] are also given.

Figure 2 shows cross sectional images of SCZ ceramic samples. The relative density of SCZ5-SCZ7.5-SCZ10 ceramics varies about 94 %, whereas in samples SCZ12.5 and SCZ15 the density slightly decreases to 91 %. According to the EDX data analysis, all elements in SCZ5-SCZ12.5 are distributed uniformly. Whereas, a clear Ca enrichment is observed in the local areas of SCZ15 sample (Fig. 2c). The presence of such areas indicates the formation of second phase Ca-enriched precipitates. These precipitates have apparently low number density, which is below the detection limit of XRD.

3.2. Thermal expansion

The results of dilatometric measurements of SCZ ceramic samples are presented in Fig. 3. The initial dilatometric dependences are shown in Fig. A2. Average TEC values for Ca-doped samarium zirconates is about $11.5 \cdot 10^{-6}$ K^{-1}, which is higher than for the conventional oxide-ion electrolyte – YSZ ($10.4 \cdot 10^{-6}$ K^{-1} [62]). It is known that with a decrease in the ionic radius of the lanthanide in $Ln_2Zr_2O_7$, the TEC values increase [60, 61]. A higher TEC values make it possible to use samarium zirconates as materials of thermal barrier coatings (TBCs) [1–6] which is not available for

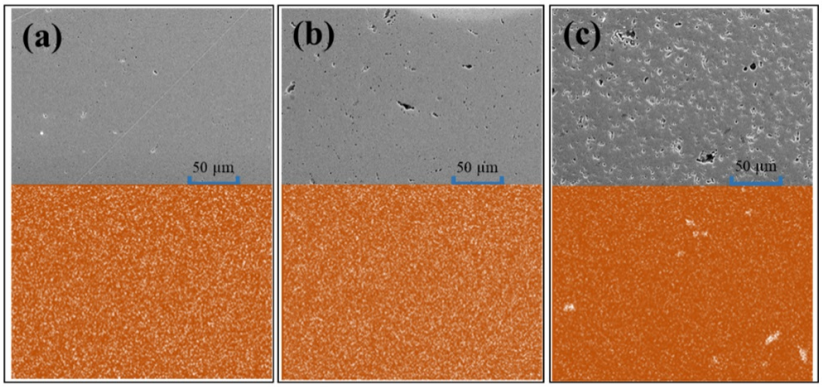

FIG. 2. Cross-sectional SEM images of SCZ5 (a), SCZ10 (b) and SCZ15 (c) along with EDX maps of Ca distribution

some other rare earth element zirconates [63]. Also, higher TEC values make the materials more compatible with SOFC electrode materials and similar electrochemical devices [64].

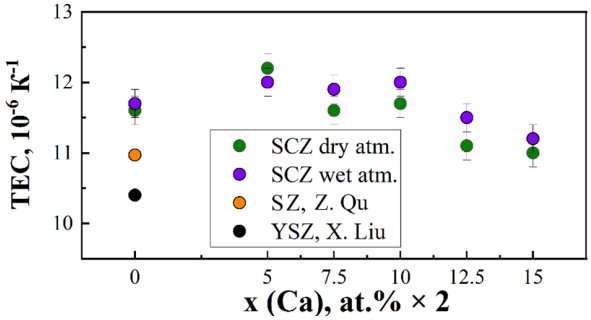

FIG. 3. Average thermal expansion coefficients (TEC) for SCZ ceramic samples obtained from dilatometry in dry ($pH_2O < 0.1$ kPa) and wet ($pH_2O = 2.8$ kPa) atmospheres. Our experimental data are compared with literature data for $Sm_2Zr_2O_7$ (SZ) [63] and yttria stabilized zirconia (YSZ) [62].

According to dilatometry data, thermal expansion of SCZ materials does not depend practically on air humidity, and the difference in the TEC in two atmospheres is at the error level. Under stepwise hydration, SCZ5 and SCZ10 samples experience a weak response to a change in humidity, because oxygen vacancies in samarium zirconates are stable to hydration (Fig. A3). Relaxation of chemical expansion occurs abruptly and quickly. It is possible that only partial surface hydration occurs.

3.3. Total conductivity and defects equilibrium

Figure 4 shows the temperature dependencies of the total conductivity for SCZ samples. SCZ5 has a systematically higher conductivity than SZ, while a further increase in Ca concentration generally leads to a decrease in conductivity. Only the conductivity of SCZ10 dominates the others in the temperature range of 800 – 900 °C. The conductivity of all doped SCZ samples is higher than that of undoped SZ at temperatures above 500 °C. Table 1 lists the apparent activation energies (E_A). SZ and SCZ5 have comparable E_A, while at higher Ca concentrations, the E_A increases markedly. In general, the increase in the E_A of materials with Ca concentration in $Sm_{2-x}Ca_xZr_2O_{7-\delta}$ is consistent with literature results [46,53]. In our case, the conductivity of SCZ5 at relatively low temperatures of about 600 °C reaches 10^{-3} S·cm^{-1} which is a record value in the series of oxide pyrochlores, even exceeding the conductivity of the most conducting phases based on doped $Gd_2Zr_2O_7$ [30–34, 49–51].

We did not find a noticeable effect of air humidity on the conductivity of the materials studied, although some researchers have considered these materials as potential proton conductors [46,65]. The air humidity has a slightly visible effect on the conductivity only at temperatures below 700 °C (Fig. 4b). It is difficult to estimate the level of proton conductivity in samarium zirconates according to our data, while we assume that the bulk proton conductivity is very small, and these materials can be successfully considered as oxygen-ion conductors.

Figure 5 shows the conductivity versus pO_2 dependence for $Sm_{2-x}Ca_xZr_2O_{7-\delta}$ ($x = 0.05, 0.1, 0.15$). A small effect of pO_2 on the conductivity is seen at all temperatures studied. Analogous dependencies can be found in the literature for $Gd_{2-x}M_xZr_2O_{7-\delta}$ (M = Li, Mg) systems [8,9]. Taken into account the specifics of disorder in the studied pyrochlore-like

TABLE 1. Apparent activation energies of total conductivity (E_{Tot}) for $Sm_{2-x}Ca_xZr_2O_{7-\delta}$ (x = 0, 0.05, 0.1, 0.15)

Composition	Activation energy of total conductivity (E_{Tot}), eV	
	Dry air, $pH_2O < 0.1$ kPa	Wet air, pH_2O = 2.8 kPa
$Sm_2Zr_2O_{7-\delta}$	0.73	—
$Sm_{1.95}Ca_{0.05}Zr_2O_{6.975}$	0.75	0.75
$Sm_{1.9}Ca_{0.1}Zr_2O_{6.95}$	0.94	0.90
$Sm_{1.85}Ca_{0.15}Zr_2O_{6.925}$	1.06	1.04

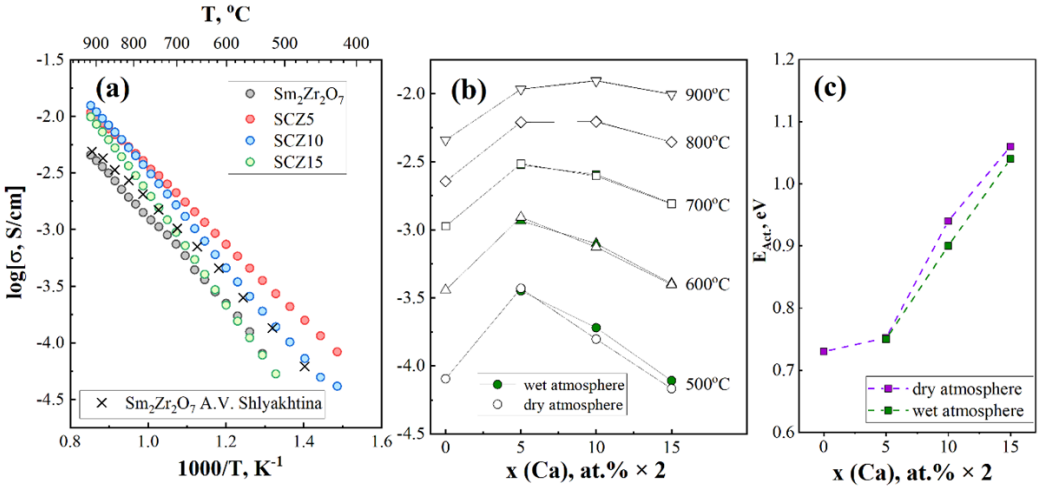

FIG. 4. The Arrenius plot of total conductivity for SCZ samples in dry air (a), isothermal dependences of total conductivity on Ca dopant concentration at different temperatures in dry and wet air (b) and apparent activation energies of total conductivity (c). Conductivity values for $Sm_2Zr_2O_7$ according to Shlyakhtina et al. [46] data are also given.

materials [22,25], several processes affecting the concentration of defects can take place. First, there are oxygen vacancies formed due to doping:

$$CaO(-SmO_{1.5}) \rightarrow Ca'_{Sm} + \frac{1}{2}V_O^{\bullet\bullet} + O_O^{\times}, \quad (1)$$

where Ca'_{Sm} are Ca atoms in Sm positions, $V_O^{\bullet\bullet}$ are oxygen vacancies, and $O_O^{\times}$ are oxygen atoms in regular lattice sites. With an increase in temperature, the probability of the formation of anti-Frenkel defects increases according to the equation:

$$O_O^{\times} \rightarrow O_O^{''} + V_O^{\bullet\bullet}, \quad (2)$$

where $O_O^{''}$ is the interstitial positions of oxygen. Oxygen vacancies formed by both (1) and (2) reactions can interact with the molecular oxygen:

$$\frac{1}{2}O_2 + V_O^{\bullet\bullet} \rightarrow O_O^{\times} + 2h. \quad (3)$$

This creates two electron holes $h^{\bullet}$. In the case of the dominance of reaction (3), the conductivity should be a linear function of $pO_2^{1/4}$. However, at 800 and 700 °C, the conductivity is linearized only in the plots $\sigma = f(pO_2^{-1/6})$ (Fig. 5d), while the $\sigma = f(pO_2^{1/4})$ dependence can be found only below 600 °C (Fig. 5e). This indicates the occurrence of several competing processes at temperatures above 700 °C. One of the side processes can be a change in the number of oxygen vacancies, for example, during reaction (2). However, Hagiwara et al. [66] showed by XRD that the occupancy of the O(8a) position in $Eu_2Zr_2O_7$ at 900 °C is even less than that at room temperature. Shehu [67] also showed by ND method a slight decrease in the occupancy of the O(8a) position at a temperature of 800 °C relative to room temperature for $Nd_{2-x}Ca_xZr_2O_{7-\delta}$.

In fact, the O(8a) site in the pyrochlore structure is often called interstitial, although this is not exactly like that. This position is free in ideal pyrochlore, for example in $La_2Zr_2O_7$ [66]. With a decrease in the ionic radius of the lanthanide, the probability of the formation of a split oxygen vacancy increases, when the oxygen atom is displaced from the O(48f)

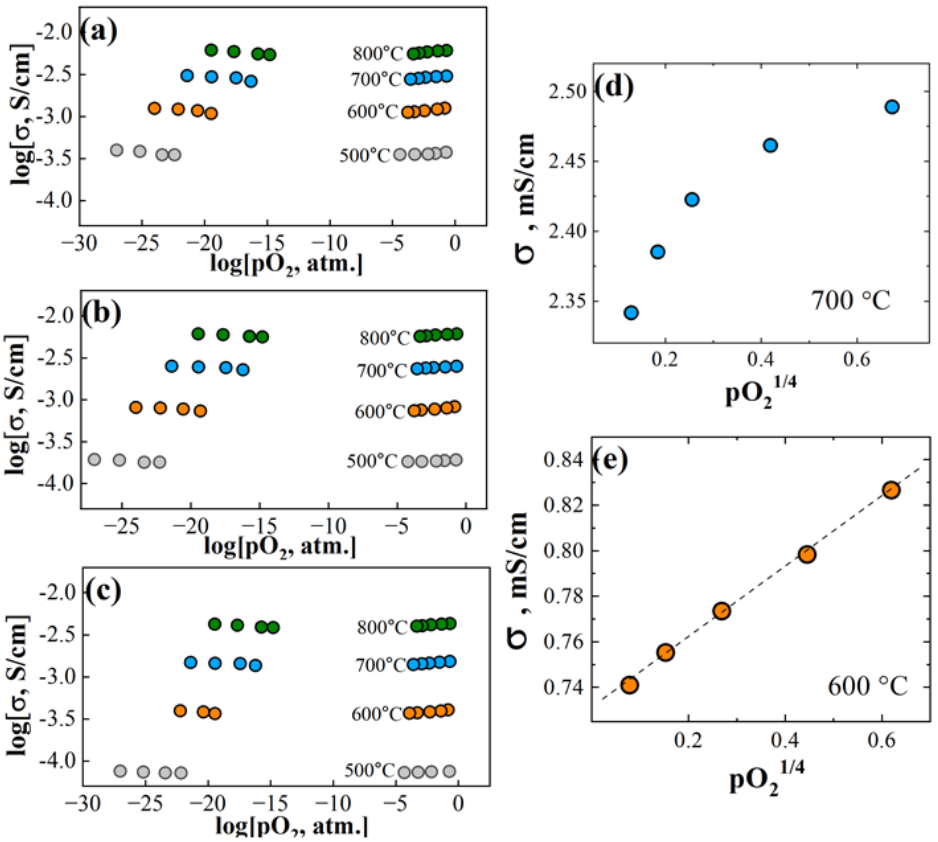

FIG. 5. Total conductivities of SCZ as a functions of the pO_2 in wet atmosphere for SCZ5 (a), SCZ10 (b), SCZ15 (c). Dependences of total conductivity as a function of $pO_2^{1/4}$ for SCZ10 at 700 °C (d) and 600 °C (e).

site towards the O(8a) site, and as a result, the interstitial oxygen atom is between two vacancies in the O(48f) sites [22]. Thus, the oxygen atom never occupies O(8a) site, but only approaches it. If the migration of an "ordinary" oxygen vacancy (at O(48f) or O(8b) sites) is preferable in the crystallographic direction (100), then the split vacancy migrates on average in the direction [111] [22]. In fact, hole migration is also anisotropic and passes along the [110] direction through the Zr and O(48f) positions [19]. This migration direction is perpendicular to the migration direction of ordinary oxygen vacancies. We can assume that the dependence of the total conductivity of SCZ on pO_2 at temperatures above 600 °C is a function not only of the concentration of electron holes but also of the concentration ratio between ordinary and split oxygen vacancies as well as the difference in their mobility due to anisotropic migration.

In contrast to the O(48f) sites, oxygen vacancies in the O(8b) site have a high energy of both formation and migration, as indicated by a number of theoretical studies [20–23]. The oxygen atom O(8b) is surrounded exclusively by A cations. It is to be expected that when the Ca dopant occupies a position in the A sublattice it contributes to the formation of an oxygen vacancy in its immediate environment, including in the O(8b) position. It is worth noting that Shehu [67] did not observe an appreciable deviation from 1 in the occupancy of O(8b) positions in $Nd_{2-x}Ca_xZr_2O_{7-\delta}$ by ND even at a very high dopant concentration ($x = 0.5$). The pair distribution function (PDF) analysis showed a decrease in the average coordination number in the Nd sublattice, but its increase for the Zr sublattice [67]. Thus, the coordination environment of all cations changes [28, 67].

It can be seen that the Ca dopant concentration has a progressive effect on disordering in SCZ, in accordance with the ideas developed by van Dijk et al. [15, 20]. Formally, the total number of oxygen vacancies increases with increasing Ca concentration which increases the pre-exponential factor of conductivity, but the vacancies are localized in unfavorable crystallographic positions which complicates their migration and increases the activation energy of conductivity.

The presence of a weak but noticeable dependence of conductivity on pO_2 in reducing atmospheres confirms the evolution of the number of oxygen vacancies in materials when oxygen leaves the interstitial positions of the material lattice, interacting with hydrogen:

$$O_O^{''} + H_2 \rightarrow H_2O + 2e^{'}. \quad (4)$$

As a result, electrons e' are generated for charge compensation, which leads to a slight increase in conductivity. These electrons are probably localized and may be the reason for the partial reduction of Sm^{3+} to Sm^{2+}. This behavior

is typical for both undoped [68] and Ca-doped samarium zirconate [46]. We additionally tested the stability of SCZ5 sample to reduction through long-term calcination in an H_2 atmosphere (Fig. A4). No signs of new phases were found, but the unit cell parameter increases noticeably from 10.583 Å after calcination in dry air at 1000 °C for 20 hours to 10.618 Å after calcination in dry hydrogen at 850 °C for 250 hours. This may be caused by an increase in the ionic radius of samarium from Sm^{3+} ($r = 1.08$ Å, CN = 8) to Sm^{2+} ($r = 1.27$ Å, CN = 8) [52].

The question remains for our case: why does a low concentration of Ca dopant (2.5 %) in $Sm_2Zr_2O_7$ increase the conductivity of the material and does not influence on the E_A. It differs from the results of Xia et al. [53], who received a clear negative reaction? We exclude the influence of sample density, since high-density samples were obtained in both our and Xia et al. [53] works. It is more likely that the difference is due to the specific features of the local structure of pyrochlores where disorder in the anion and cation sublattices is closely related [21, 24–28]. The dopant causes a change in the coordination environment in both A and B sublattices [28, 67]. Van Dijk et al. [15, 20] argue that the oxygen vacancy has the lowest energy when passing between O(48f) positions near the O(8a) position which is essentially identical to the mechanism of migration of a split vacancy. Probably, disruption of such optimal pathways causes a decrease in the mobility of oxygen ions. Unlike the works [46, 53], where the SCZ materials were obtained by a solid-phase reaction, in our case, a solution synthesis method with a precursor combustion stage was used. This condition affects the proportion of antistructural defects, as well as the distribution of Ca dopant over the A and B sublattices. It should be expected that the stages of high-temperature combustion and subsequent high-temperature annealing contribute to greater pyrochlore ordering and the formation of a smaller number of antisite pairs, and the solution stage of synthesis promotes the localization of the Ca dopant in the A sublattice. The effect of annealing temperature on the degree of ordering of the pyrochlore structure was shown in the paper [58]. Thus, a small dopant concentration apparently promotes the formation of an increased number of "free" oxygen vacancies and the favorable migration paths are not interrupted. An increased concentration of the dopant causes a violation of the optimal coordination of A and B cations which leads to high energy consumption for the migration of oxygen ions. We believe that an ND study could directly show the occupancy of oxygen positions, unfortunately, ND is difficult for Sm due to its high neutron absorption cross sections. According to ND data for $Nd_{2-x}Ca_xZr_2O_{7-\delta}$ [67], the occupancy of the O(8a) position increases noticeably with the dopant concentration and slightly decreases when the material is heated to 800 °C. In addition, Shehu [67] also found a clear increase in the activation energy of conductivity with increasing dopant concentration.

The above allows us to make two general assumptions:

(1) The migration of a split oxygen vacancy, despite the low energy barrier, is disrupted at high defect concentrations. This should also be related to the occupancy of O(8a) positions. A significant change in the coordination environment of cations disrupts the optimal migration routes of oxygen ions.
(2) If the localization of the Ca dopant is preferable in the A position of $Sm_2Zr_2O_7$, and accordingly, the effect only on coordination in the A sublattice occurs, then this contributes to the formation of energetically favorable oxygen vacancies with low migration activation energy. If part of the dopant ends up in the B position, this will lead to a more significant mismatch of ionic radii between Ca and Zr. The oxygen ion, when migrating, will need to overcome a higher energy barrier in order to change the local coordination of the B cation.

3.4. Grains boundaries state

Since polycrystalline ceramics are under study, one might suspect that the trends in material conductivity discussed above are not related to the equilibrium model of defects in the grain volume, but to the contribution of grain boundary (GB) conductivity. EIS was used to clarify this. Unfortunately, EIS measurements were carried out at lower temperatures compared to the 4-probe method in order to be able to observe the high-frequency response of the impedance spectrum. Fig. 6a shows typical impedance spectra at 350 °C for ceramic samples SCZ5 and SCZ10. A large semicircle emerging from the origin, as well as an additional semicircle, are clearly visible. It should be noted that the analysis may complicate the response from the electrode, so we achieved the lowest resistance of the electrodes by activating them, as was indicated in the experimental section. DRT analysis was used to separate the contributions of relaxation processes on the impedance spectra. Fig. 6b shows the results of DRT analysis at 350 °C. High-frequency processes with characteristic relaxation times of $\sim 10^{-5.5}$ s and capacitances of $\sim 10^{-11}$ F correspond to the bulk resistance. Low-frequency processes with relaxation times of about 10^{-4} s and capacitances of $\sim 10^{-9}$ F can correspond to the GB resistance. The relaxation times of the GB process for SCZ10 are systematically slightly longer than for SCZ5 for all temperatures studied. At the same time, the relaxation times of the bulk process are close for the two samples.

It is worth noting that the resistance of the GB process observed from the impedance spectra is apparent and, before calculating the specific values, it is lower than the bulk one for the both samples. Under the approximation of equality of dielectric constants of bulk and GB [69], the specific GB resistance can be expressed through the ratio of process capacitances:

$$R^*_{\mathrm{gb}} = R_{\mathrm{gb}} \cdot \frac{C_{\mathrm{gb}}}{C_{\mathrm{bulk}}}. \tag{5}$$

After recalculation, the specific GB conductivity turns out to be noticeably lower than the bulk resistance.

Figure 6c shows the temperature dependences of the bulk and GB conductivity. The dependences of the bulk conductivity are in good agreement with the higher temperature region of conductivity determined by the 4-probe method (Fig. 4a). More importantly, the apparent activation energies of grain volume conductivity are in agreement with higher temperature data which makes our previous discussions about the equilibrium model of defects in the materials under study valid.

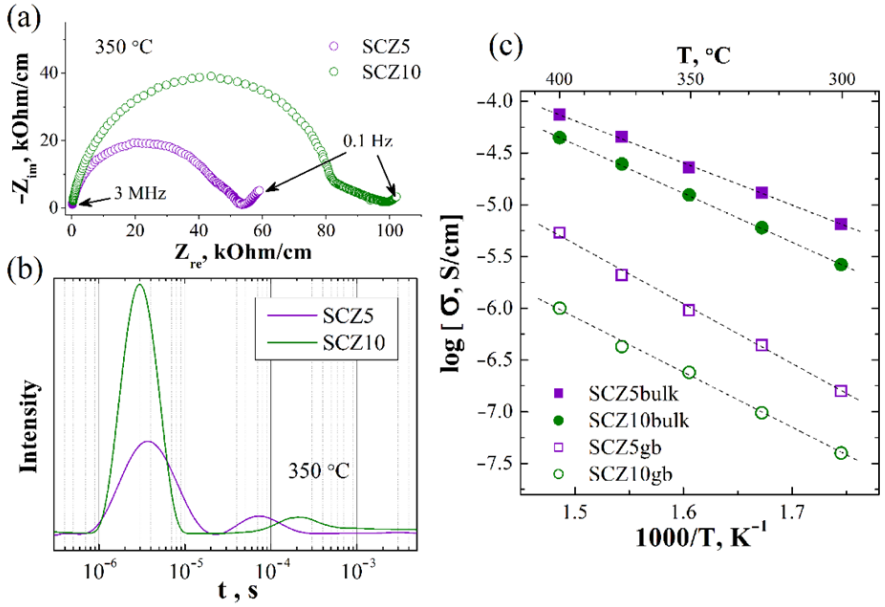

FIG. 6. (a) EIS results, (b) DRT spectra and (c) temperature dependencies of bulk and grain boundaries conductivities of SCZ5 and SCZ10 ceramics

To directly confirm or deny formation of single pyrochlore structure at sub-grain scale, we investigate the GB chemistry for SCZ5 and SCZ10 samples. Fig. 7 shows typical bright-field TEM (BF TEM) images and corresponding selected area diffraction (SAED) patterns of SCZ5 and SCZ10 samples. Both samples contained no visible precipitates. In addition, SAED patterns of the SCZ5 and the SCZ10 samples, clearly demonstrate that the local crystal structure of both samples fully matches the cubic phase of $Sm_2Zr_2O_7$, in the PDF-2 database (ICSD 261415) as follows: the space group $Fd\bar{3}m$ (227).

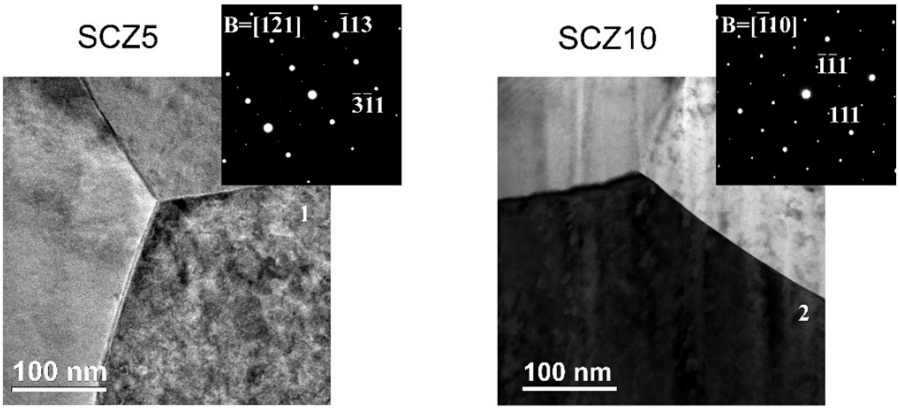

FIG. 7. BF TEM images and corresponding SAED patterns of SCZ5 and SCZ10 ceramics cross-sections in the triple junction area

Figure 8 shows the element concentration profiles across the GB for samples SCZ5 and SCZ10 which indicate a uniform distribution of all elements. This contrasts with the results for $La_{2-x}Ca_xZr_2O_{7-\delta}$ which show clear segregation of the Ca dopant to the GB [43]. Fig. A5 provides the EDX compositional maps of SCZ5 and SCZ10 samples obtained in the triple junction region using the scanning transmission electron microscopy regime (STEM-EDX). Based on the analysis of STEM-EDX compositional maps, both samples under study contain homogeneously distributed Sm, Ca, Zr and O; neither Ca precipitates inside grains, nor Ca segregation at the GB were formed in these samples.

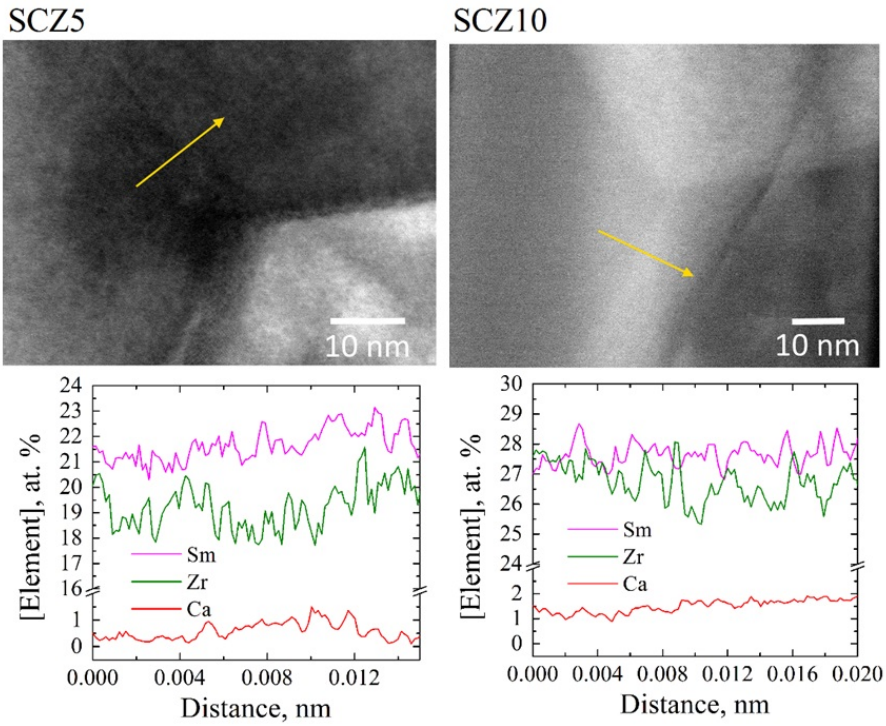

FIG. 8. HAADF images of SCZ ceramics cross-sections of in the region of the triple junction of grains with EDX-profiles across the grain boundaries

Thus, from the totality of the results, it can be expected that the conductivity trends at high temperatures are observed for both bulk and GB. Disorder at GB in pyrochlores is known to occur due to an increased number of antisite pairs, although this effect becomes less significant as cationic disorder in the bulk increases [70]. Apparently, GB, having a similar structure and composition to the bulk, exhibits a similar model of defect equilibrium and only the usual space charge is realized [69].

4. Conclusion

In this work, we obtained high-density (> 95 %) ceramic materials based on $Sm_2Zr_2O_7$ by combustion method. It was the use of nanoscale pre-ceramic powders that ensured the formation of a given microstructure of the studied samples. We investigated the effect of acceptor doping in $Sm_2Zr_2O_7$ with a pyrochlore structure on the model of defect formation and conductivity. The low concentration of Ca dopant in the Sm sublattice increases ionic conductivity and almost does not reduce the activation energy (E_A), which makes $Sm_{1.95}Ca_{0.05}Zr_2O_{7-\delta}$ one of the most highly conductive oxide pyrochlores. The coexistence of intrinsic and impurity defects in $Sm_{2-x}Ca_xZr_2O_{7-\delta}$ gradually impairs ion transport at high doping levels. This leads to high E_A due to disruption of the optimal route of the oxygen ions migration which is typical for pyrochlore-type materials. Apparently, the localization of Ca predominantly in the Sm sublattice, which is a consequence of the solution synthesis of materials used, contributes to less distortion of the coordination environment of cations and an increased number of oxygen vacancies, simultaneously. This leads to an increase in conductivity without negatively affecting the E_A. Also, the influence of grain boundaries (GB) on the conductivity was tested using impedance spectroscopy. Transmission electron microscopy (TEM) shows the purity of the GB, so it is only the space charge that causes the reduced conductivity of the GB. $Sm_{1.95}Ca_{0.05}Zr_2O_{7-\delta}$ has been shown to have good chemical stability and a coefficient of thermal expansion (TEC) of 12 ppm K^{-1} which is higher than YSZ and provides better compatibility with electrode materials. This allows it to be used as a highly stable oxygen electrolyte in electrochemical devices.

Appendix

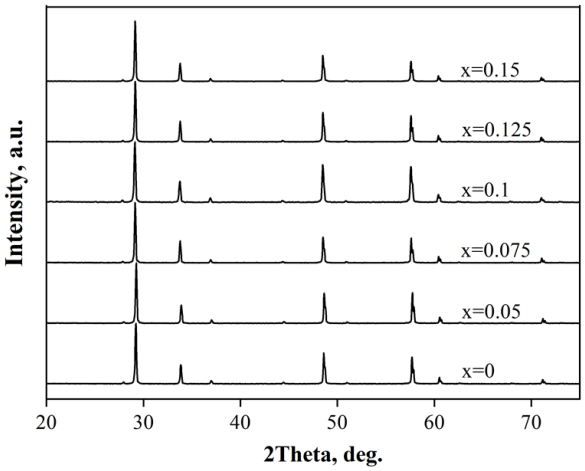

FIG. A1. XRD patterns for $Sm_{2-x}Ca_xZr_2O_{7-\delta}$ ($x = 0$; 0.05; 0.075; 0.1; 0.125; 0.15) powders calcined at 1000 °C for 20 hours in dry air

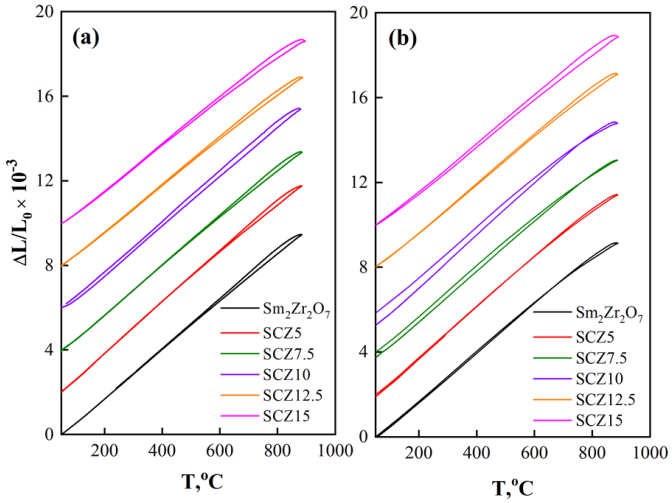

FIG. A2. Temperature dependencies of relative linear expansion and narrowing for $Sm_{2-x}Ca_xZr_2O_{7-\delta}$ ($x = 0$; 0.05; 0.075; 0.1; 0.125; 0.15) dry (a) and wet (b) atmospheres

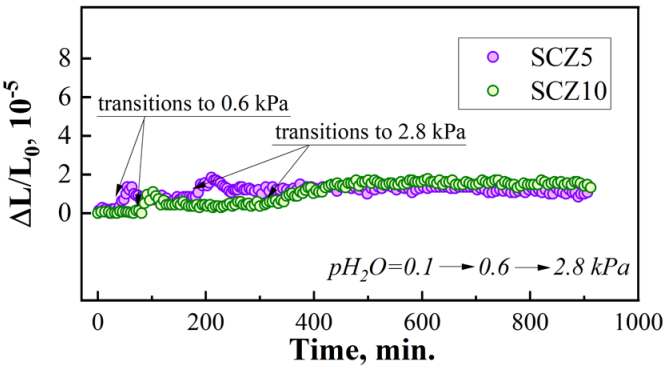

FIG. A3. Chemical expansion of SCZ5 and SCZ10 samples during the transition from a dry atmosphere ($pH_2O \approx 0.1$ kPa) to humidified atmospheres (pH_2O = 0.6, 2.8 kPa) at a constant temperature $T = 600$ °C

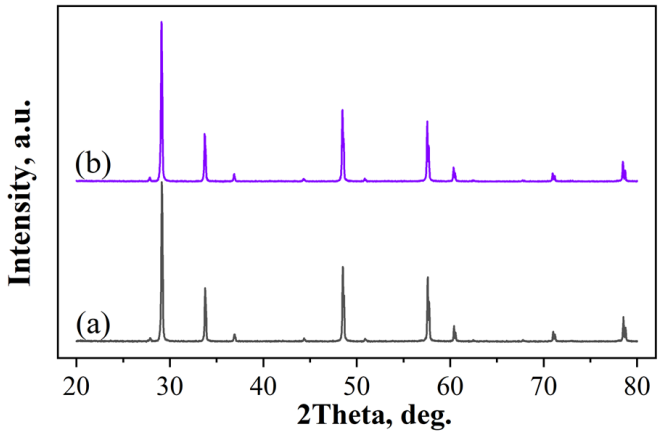

FIG. A4. XRD patterns of the SCZ5 sample before (a) and after (b) exposure in hydrogen (250 hours) at 850 °C

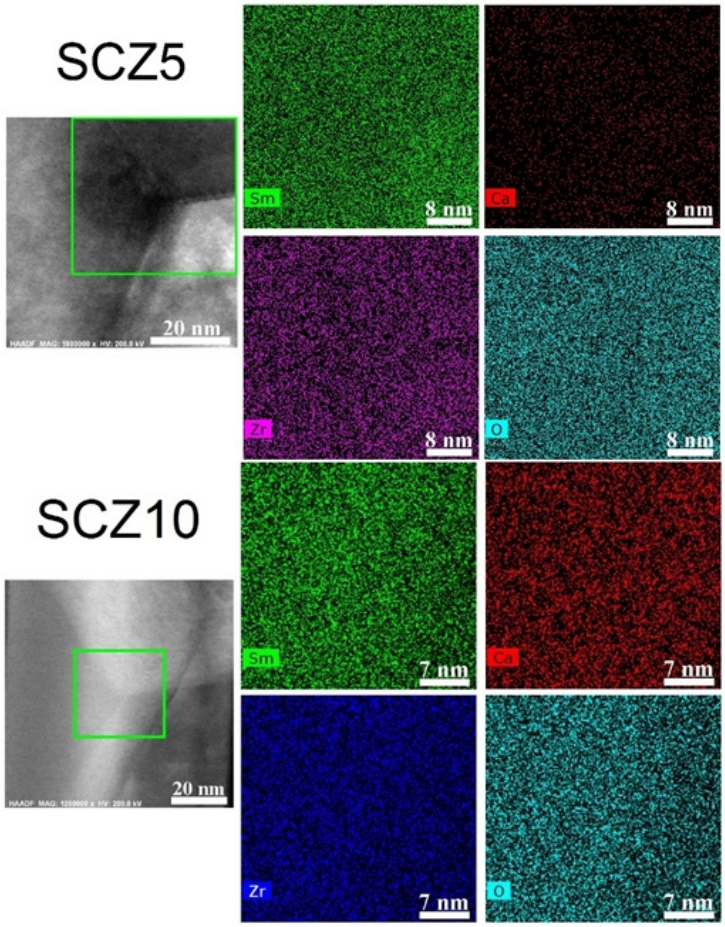

FIG. A5. HAADF and SAED cross-sectional images of SCZ5 and SCZ10 samples in the region of the triple junction of grains with STEM-EDX maps of elements distribution

References

[1] Wu J., Wei X., Padture N.P., Klemens P.G., Gell M., Garcia E., Miranzo P., Osendi M.I. Low-Thermal-Conductivity Rare-Earth Zirconates for Potential Thermal-Barrier-Coating Applications. *J. Am. Ceram. Soc.*., 2002, **85** (12), P. 3031–3035.

[2] Wan C.L., Pan W., Xu Q., Qin Y.X., Wang J.D., Qu Z.X., Fang M.H. Effect of point defects on the thermal transport properties of $(La_xGd_{1-x})_2Zr_2O_7$: Experiment and theoretical model. *Phys. Rev. B*, 2006, **74** (14), 144109.

[3] Shin D., Shin H.G., Lee H., Thermodynamic investigation of the $(La_{1-x}Gd_x)_2Zr_2O_7$ pyrochlore phase. *Calphad*, 2014, **45**, P. 27–32.

[4] Schmitt M.P., Rai A.K., Bhattacharya R., Zhu D., Wolfe D.E. Multilayer thermal barrier coating (TBC) architectures utilizing rare earth doped YSZ and rare earth pyrochlores. *Surf. Coat. Technol.*, 2014, **251**, P. 56–63.

[5] Zhang J., Guo X., Jung Y.G., Li L., Knapp J. Lanthanum zirconate based thermal barrier coatings: A review. *Surf. Coat. Technol.*, 2017, **323**, P. 18–29.

[6] Mathanbabu M., Thirumalaikumarasamy D., Thirumal P., Ashokkumar M. Study on thermal, mechanical, microstructural properties and failure analyses of lanthanum zirconate based thermal barrier coatings: A review. *Mater. Today Proc.*, 2021, **46** (17), P. 7948–7954.

[7] Anokhina I.A., Animitsa I.E., Buzina A.F., Nokhrin S.S., Zaikov Y.P., Voronin V.I., Vykhodets, V.B. Kurennykh, T.E. Kazakova, V.N. Electrical properties of Li+-substituted solid solutions based on $Gd_2Zr_2O_7$. *Russ. J. Phys. Chem. A*, 2021, **95**, P. 2426–2431.

[8] Anokhina I.A., Animitsa I.E., Voronin V.I., Vykhodets V.B., Kurennykh T.E., Molchanova N.G., Vylkov A.I., Dedyukhin A.E., Zaikov Y.P. The structure and electrical properties of lithium doped pyrochlore $Gd_2Zr_2O_7$. *Ceram. Int.*, 2021, **47**, P. 1949–1961.

[9] Anokhina I., Pavlenko O., Proskurnina N., Dedyukhin A., Animitsa I. The $Gd_{2-x}Mg_xZr_2O_{7-x/2}$ Solid Solution: Ionic Conductivity and Chemical Stability in the Melt of LiCl–Li_2O. *Materials*, 2022, **15**, 4079.

[10] Sickafus K.E., Mimervini L., Grimes R.W., Valdez J.A., Ishimaru M., Li F., McClellan K.J. Hartmann, T. Radiation tolerance of complex oxides. *Science*, 2000, **289** (5480), P. 748–751.

[11] Wang S.X., Begg B.D., Wang L.M., Ewing R.C., Weber W.J., Govidan Kutty K.V. Radiation stability of gadolinium zirconate: a waste form for plutonium disposition, *J. Mater. Res.*, 1999, **14**, P. 4470–4473.

[12] Wuensch B.J., Eberman K.W., Heremans C., Ku E.M., Onnerud P., Yeo E.M.E., Haile S.M., Stalick J.K., Jorgensen J.D. Connection between oxygen-ion conductivity of pyrochlore fuel-cell materials and structural change with composition and temperature. *Solid State Ion*, 2000, **129**, P. 111–133.

[13] Anantharaman A.P., Dasari H.P. Potential of pyrochlore structure materials in solid oxide fuel cell applications. *Ceram. Int.*, 2021, **47**, P. 4367–4388.

[14] Mandal B.P., Tyagi A.K. Ionic conductivity in materials with a pyrochlore structure. In *Pyrochlore Ceramics: Properties, Processing, and Applications*, *Elsevier Series on Advanced Ceramic Materials*, Chowdhury A., Ed., Elsevier: Amsterdam, Netherlands, 2022, **7**, P. 277–294.

[15] Van Dijk M.P., Burggraaf A.J., Cormack A.N., Catlow C.R.A. Defect structures and migration mechanisms in oxide pyrochlores. *Solid State Ion*, 1985, **17** (2), P. 159–167.

[16] Tabira Y., Withers R., Thompson J., Schmid S. Structured diffuse scattering as an indicator of inherent cristobalite-like displacive flexibility in the rare earth zirconate pyrochlore $La_\delta Zr_{1-\delta}O_{2-\delta/2}$, $0.49 < \delta < 0.51$. *J. Solid State Chem.*, 1999, **142**, P. 393–399.

[17] Whittle K.R., Cranswick L.M.D., Redfern S.A.T., Swainson I.P., Lumpkin G.R. Lanthanum pyrochlores and the effect of yttrium addition in the systems $La_{2-x}Y_xZr_2O_7$ and $La_{2-x}Y_xHf_2O_7$. *J. Solid State Chem.*, 2009, **182**, P. 442–450.

[18] Blanchard P.E.R., Clements R., Kennedy B.J., Ling C.D., Reynolds E., Avdeev M., Stampfl A.P.J., Zhang Z., Jang L.Y. Does local disorder occur in the pyrochlore zirconates? *Inorg. Chem.*, 2012, **51**, P. 13237–13244.

[19] Hagiwara T., Yamamura H., Nishino H. Relationship between oxide-ion conductivity and ordering of oxygen vacancy in the $Ln_2Zr_2O_7$ (Ln = La, Nd, Eu) system having a pyrochlore composition. *IOP Conf. Series: Materials Science and Engineering*, 2011, **18**, 132003.

[20] Van Dijk M.P., de Vries K.J., Burggraaf A.J. Oxygen ion and mixed conductivity in compounds with the fluorite and pyrochlore structure. *Solid State Ion*, 1983, **9**&**10**, P. 913–920.

[21] Wilde P.J., Catlow C.R.A. Defects and diffusion in pyrochlore structured oxides. *Solid State Ion*, 1998, **112**, P. 173–183.

[22] Pirzada M., Grimes R.W., Minervini L., Maguire J.F., Sickafus K.E. Oxygen migration in $A_2B_2O_7$ pyrochlores. *Solid State Ion*, 2001, **140**, P. 201–208.

[23] Nyman B.J., Björketun M.E., Wahnström G. Substitutional doping and oxygen vacancies in $La_2Zr_2O_7$ pyrochlore oxide. *Solid State Ion*, 2011, **189**, P. 19–28.

[24] Li Y., Kowalski P.M. Energetics of defects formation and oxygen migration in pyrochlore compounds from first principles calculations, *J. Nucl. Mater.*, 2018, **505**, P. 255–261.

[25] Minervini L., Grimes R.W., Sickafus K.E. Disorder in pyrochlore oxides. *J. Am. Ceram. Soc.*, 2000, **83**, P. 1873–1878.

[26] Shlyakhtina A.V., Savvin S.N., Levchenko A.V., Knotko A.V., Fedtke P., Busch A., Barfels T., Wienecke M., Shcherbakova L.G. Study of bulk and grain-boundary conductivity of $Ln_{2+x}Hf_{2-x}O_{7-\delta}$ (Ln = Sm–Gd, $x = 0, 0.096$) pyrochlores. *J. Electroceram.*, 2010, **24**, P. 300–307.

[27] Li Y., Kowalski P.M., Beridze G., Birnie A.R., Finkeldei S., Bosbach D. Defect formation energies in $A_2B_2O_7$ pyrochlores. *Scr. Mater.*, 2015, **107**, P. 18–21.

[28] Marlton F.P., Zhang Z., Zhang Y., Proffen T.E., Ling C.D., Kennedy B.J. Lattice Disorder and Oxygen Migration Pathways in Pyrochlore and Defect-Fluorite Oxides. *Chem. Mater.*, 2021, **33**, P. 1407–1415.

[29] Zhang F.X., Lang M., Ewing R.C. Atomic disorder in $Gd_2Zr_2O_7$ pyrochlore. *Appl. Phys. Lett.*, 2015, **106**, 191902.

[30] Díaz-Guillén J.A., Díaz-Guillén M.R., Padmasree K.P., Fuentes A.F., Santamaría J., León C. High ionic conductivity in the pyrochlore-type $Gd_{2-y}La_yZr_2O_7$ solid solution ($0 \leq y \leq 1$). *Solid State Ion*, 2008, **179**, P. 2160–2164.

[31] Mandal B.P., Deshpande S.K., Tyagi A.K. Ionic conductivity enhancement in $Gd_2Zr_2O_7$ pyrochlore by Nd doping. *J. Mater. Res.*, 2008, **23**, P. 911–916.

[32] Moreno K.J., Fuentes A.F., García-Barriocanal J., León C., Santamaría J. Mechanochemical synthesis and ionic conductivity in the $Gd_2(Sn_{1-y}Zr_y)_2O_7$ ($0 \leq y \leq 1$) solid solution. *J. Solid State Chem.*, 2006, **179**, P. 323–330.

[33] Díaz-Guillén M.R., Moreno K.J., Díaz-Guillén J.A., Fuentes A.F., García-Barriocanal J., Santamaría J., León C. Dynamics of mobile oxygen ions in disordered pyrochlore-type oxide-ion conductors. *Defect and Diffusion Forum*, 2009, **289–292**, P. 347–354.

[34] Díaz-Guillén J.A., Fuentes A.F., Díaz-Guillén M.R., Almanza J.M., Santamaría J., León, C. The effect of homovalent A-site substitutions on the ionic conductivity of pyrochlore-type $Gd_2Zr_2O_7$. *J. Power Sources*, 2009, **186**, P. 349–352.

[35] Tuller H.L. Oxygen ion conduction and structural disorder in conductive oxides. *J. Phys. Chem. Solids*, 1994, **55** (12), P. 1393–1404.

[36] Omata T., Otsuka-Yao-Matsuo S. Electrical properties of proton-conducting Ca^{2+}-doped $La_2Zr_2O_7$ with a pyrochlore-type structure. *J. Electrochem. Soc.*, 2001, **148** (6), P. 252–261.

[37] Omata T., Ikeda K., Tokashiki R., Otsuka-Yao-Matsuo S. Proton solubility for $La_2Zr_2O_7$ with a pyrochlore structure doped with a series of alkaline-earth ions. *Solid State Ion*, 2004, **167**, P. 389–397.
[38] Huo D., Gosset D., Siméone D., Baldinozzi G., Khodja H., Villeroy B., Surblé S. Influence of sintering methods on microstructure and ionic conductivity of $La_{1.95}Sr_{0.05}Zr_2O_{6.975}$ synthesized by co-precipitation. *Solid State Ion*, 2015, **278**, P. 181–185.
[39] Huo D., Baldinozzi G., Siméone D., Khodja H., Surblé S. Grain size-dependent electrical properties of $La_{1.95}Sr_{0.05}Zr_2O_{7-\delta}$ as potential Proton Ceramic Fuel Cell electrolyte. *Solid State Ion*, 2016, **298**, P. 35–43.
[40] Antonova E.P., Ananyev M.V., Farlenkov A.S., Tropin E.S., Khodimchuk A.V., Porotnikova N.M. Phase equilibria, water dissolution, and peculiarities of charge transfer in Ca-doped $La_2Zr_2O_{7-\alpha}$. *Russ. J. Electrochem.*, 2017, **53**, P. 651–657.
[41] Antonova E.P., Farlenkov A.S., Tropin E.S., Eremin V.A., Khodimchuk A.V., Ananyev M.V. Oxygen isotope exchange, water uptake and electrical conductivity of Ca-doped lanthanum zirconate. *Solid State Ion*, 2017, **306**, P. 112–117.
[42] Farlenkov A.S., Khodimchuk A.V., Eremin V.A., Tropin E.S., Fetisov A.V., Shevyrev N.A., Leonidov I.I., Ananyev M.V. Oxygen isotope exchange in doped lanthanum zirconates. *J. Solid State Chem.*, 2018, **268**, P. 45–54.
[43] Vorotnikov V.A., Belyakov S.A., Plekhanov M.S., Stroeva A.Yu., Lesnichyova A.S., Zhigalina O.M., Khmelenin D.N., Àtanovà A.V., Basu V.G., Kuzmin A.V. Proton transfer in $La_{2-x}Ca_xZr_2O_{7-\delta}$ pyrochlores: Reasons for limited water uptake and high grain boundary conductivity. *Ceram. Int.*, 2022, **48**, P. 35166–35175.
[44] Fournier T., Nots J.Y., Muller J., Joubert J.C. Conductive ionique des phases de type pyrochlore $Gd_{2-x}Ca_xZr_2O_{7-x/2}$ and $Gd_2Zr_{2-x}Sc_xO_{7-x/2}$. *Solid State Ion*, 1985, **15**, P. 71–74.
[45] Zhong F., Zhao J., Shi L., Xiao Y., Cai G., Zheng Y., Long J. Alkaline-earth metals-doped pyrochlore $Gd_2Zr_2O_7$ as oxygen conductors for improved NO_2 sensing performance. *Sci. Rep.*, 2017, **7**, 4684.
[46] Shlyakhtina A.V., Abrantes J.C.C., Gomes E., Lyskov N.V., Konysheva E.Y., Chernyak S.A., Kharitonova E.P., Karyagina O.K., Kolbanev I.V., Shcherbakova L.G. Evolution of Oxygen–Ion and Proton Conductivity in Ca-Doped $Ln_2Zr_2O_7$ (Ln = Sm, Gd), Located Near Pyrochlore–Fluorite Phase Boundary. *Materials*, 2019, **12**, 2452.
[47] Kuzmin A.V., Stroeva A.Yu, Gorelov V.P., Novikova Yu.V., Lesnichyova A.S., Farlenkov A.S., Khodimchuk A.V. Synthesis and characterization of dense proton-conducting $La_{1-x}Sr_xScO_{3-\delta}$ ceramics. *Hydrogen Energy*, 2019, **44**, P. 1130–1138.
[48] Jiang L., Wang C., Wang J., Liu F., You R., Lv S., Zeng G., Yang Z., He J., Liu A., et al. Pyrochlore Ca-doped $Gd_2Zr_2O_7$ solid state electrolyte type sensor coupled with ZnO sensing electrode for sensitive detection of HCHO. *Sens. Actuators B Chem.*, 2020, **309**, 127768.
[49] Liu Z.G., Ouyang J.H., Zhou Y., Xia X.L. Effect of Sm substitution for Gd on the electrical conductivity of fluorite-type $Gd_2Zr_2O_7$. *J. Power Sources*, 2008, **185** (2), P. 876–880.
[50] Liu Z., Ouyang J., Sun K., Zhou Y. Effect of CaO addition on the structure and electrical conductivity of the pyrochlore-type $GdSmZr_2O_7$. *Ceram. Int.*, 2012, **38**, P. 2935–2941.
[51] Liu Z.-G., Ouyang J.-H., Sun K.-N., Zhou Y. Influence of magnesia doping on structure and electrical conductivity of pyrochlore type $GdSmZr_2O_7$. *Adv. Appl. Ceram.*, 2012, **111**, P. 214–219.
[52] Shannon R.D. Revised effective ionic radii and systematic studies of interatomic distances in halides and chalcogenides. *Acta Cryst. A*, 1976, **32**, P. 751–767.
[53] Xia X.-L., Ouyang J.-H., Liu Z.-G. Influence of CaO on structure and electrical conductivity of pyrochlore-type $Sm_2Zr_2O_7$. *J. Power Sources*, 2009, **189**, P. 888–893.
[54] Kovrova A.I., Gorelov V.P. Characteristics of Pt electrode activated by $Tb_{1-x}Ce_xO_{2-\alpha}$ films in contact with ZrO_2 + 10 mol % Y_2O_3 electrolyte. *Russ. J. Electrochem.*, 2019, **55**, P. 132–136.
[55] Wan T.H., Saccoccio M., Chen C., Ciucci F. Influence of the discretization methods on the distribution of relaxation times deconvolution: implementing radial basis functions with DRTtools. *Electrochim. Acta*, 2015, **184**, P. 483–499.
[56] Gavrilyuk A.L., Osinkin D.A., Bronin D.I. The use of Tikhonov regularization method for calculating the distribution function of relaxation times in impedance spectroscopy. *Russ. J. Electrochem.*, 2017, **53**, P. 575–588.
[57] Schlüter N., Ernst S., Schröder U. Finding the Optimal Regularization Parameter in Distribution of Relaxation Times Analysis. *ChemElectroChem*, 2019, **6** (24), P. 6027–6037.
[58] Yastrebtsev A.A., Popov V.V., Menushenkov A.P., Beskrovnyi A.I., Neov D.S., Shchetinin I.V., Ponkratov K.V. Comparative neutron and X-ray diffraction analysis of anionic and cationic ordering in rare-earth zirconates (Ln = La, Nd, Tb, Yb, Y). *J. Alloys Compd.*, 2020, **832**, 154863.
[59] Uno M., Kosuga A., Okui M., Horisaka K., Muta H., Kurosaki K., Yamanaka S. Photoelectrochemical study of lanthanide zirconium oxides, $Ln_2Zr_2O_7$ (Ln = La, Ce, Nd and Sm). *J. Alloys Compd.*, 2006, **420**, P. 291–297.
[60] Govindan Kutty, K.V., Rajagopalan, S., Mathews, C.K., Varadaraju, U.V. Thermal expansion behavior of some rare earth oxide pyrochlores. *Mater. Res. Bull.*, 1994, **29** (7), P. 759–766.
[61] Shimamura K., Arima T., Idemitsu K., Inagaki Y. Thermophysical Properties of Rare-Earth-Stabilized Zirconia and Zirconate Pyrochlores as Surrogates for Actinide-Doped Zirconia. *Int. J. Thermophys.*, 2007, **28**, P. 1074–1084.
[62] Liu X.Y., Xu Z.H., Liang G.Y. Comparative study of the sintering behaviors between YSZ and LZ/YSZ composite. *Mater. Lett.*, 2017, **191**, P. 108–111.
[63] Qu Z., Wan C., Pan W. Thermal expansion and defect chemistry of MgO-doped $Sm_2Zr_2O_7$. *Chem. Mater.*, 2007, **19**, P. 4913–4918.
[64] Nikonov A.V., Kuterbekov K.A., Bekmyrza K.Z., Pavzderin N.B. A brief review of conductivity and thermal expansion of perovskite-related oxides for SOFC cathode. *Eurasian J. Phys. Funct. Mater.*, 2018, **2** (3), P. 274–292.
[65] Eurenius K.E.J., Ahlberg E., Knee C.S. Role of B-site ion on proton conduction in acceptor-doped $Sm_2B_2O_{7-\delta}$ (B = Ti, Sn, Zr and Ce) pyrochlores and C-type compounds. *Dalton Trans.*, 2011, **40**, P. 3946–3954.
[66] Hagiwara T., Nomura K., Kageyama H. Crystal structure analysis of $Ln_2Zr_2O_7$ (Ln = Eu and La) with a pyrochlore composition by high-temperature powder X-ray diffraction. *J. Ceram. Soc. Jpn.*, 2017, **125**, P. 65–70.
[67] Shenu A. Structural Analysis and Its Implications for Oxide ion Conductivity of Lanthanide Zirconate Pyrochlores. PhD Thesis, School of Biological and Chemical Sciences, Queen Mary University of London, London, UK, 2018.
[68] Shlyakhtina A.V., Belov D.A., Knotko A.V., Kolbanev I.V., Streletskii A.N., Karyagina O.K., Shcherbakova L.G. Oxygen Interstitial and Vacancy Conduction in Symmetric $Ln_{2\pm x}Zr_{2\pm x}O_{7\pm x/2}$ (Ln = Nd, Sm) Solid Solutions. *Inorg. Mater.*, 2014, **50** (10), P. 1035–1049.
[69] Guo X., Maier J. Grain Boundary Blocking Effect in Zirconia: A Schottky Barrier Analysis. *J. Electrochem. Soc.*, 2001, **148**, E121–E126.
[70] Perriot R., Dholabhai P.P., Uberuaga B.P. Disorder-induced transition from grain boundary to bulk dominated ionic diffusion in pyrochlores. *Nanoscale*, 2017, **9**, P. 6826–6836.

Submitted 25 November 2023; revised 1 February 2024; accepted 6 February 2024

Information about the authors:

Vladimir A. Vorotnikov – Institute of Chemistry and Ecology, Vyatka State University, Kirov 610000, Russia; Institute of Solid-State Chemistry and Mechanochemistry SB RAS, Novosibirsk, 630090, Russia; ORCID 0000-0002-0247-6198; vorotnikov130@mail.ru

Semyon A. Belyakov – Institute of High-Temperature Electrochemistry UB RAS, Yekaterinburg 620137, Russia; ORCID 0000-0001-9237-8307; bca2@mail.ru

Alexey V. Ivanov – Institute of Chemistry and Ecology, Vyatka State University, Kirov 610000, Russia; Institute of Solid-State Chemistry and Mechanochemistry SB RAS, Novosibirsk, 630090, Russia; ORCID 0000-0002-7666-831X; alehaww@gmail.com

Yulia V. Novikova – Institute of High-Temperature Electrochemistry UB RAS, Yekaterinburg 620137, Russia; ORCID 0000-0002-0369-3274; meryl18@mail.ru

Anna Yu. Stroeva – Institute of Chemistry and Ecology, Vyatka State University, Kirov 610000, Russia; ORCID 0000-0002-6772-3321; stroevaanna@yandex.ru

Vadim V. Grebenev – Shubnikov Institute of Crystallography of Federal Scientific Research Centre "Crystallography and Photonics" of the RAS, Moscow 119333, Russia; ORCID 0000-0002-5484-4642; vadim_grebenev@mail.ru

Dmitry N. Khmelenin – Shubnikov Institute of Crystallography of Federal Scientific Research Centre "Crystallography and Photonics" of the RAS, Moscow 119333, Russia; ORCID 0000-0003-0894-5087; xorrunn@gmail.com

Olga V. Emelyanova – Shubnikov Institute of Crystallography of Federal Scientific Research Centre "Crystallography and Photonics" of the RAS, Moscow 119333, Russia; ORCID 0000-0003-3951-8985; eolga@bk.ru

Maksim S. Plekhanov – Institute of Crystallography, RWTH Aachen University, Aachen 52066, Germany; ORCID 0000-0002-2701-4619; plexanovmax@mail.ru

Anton V. Kuzmin – Institute of Chemistry and Ecology, Vyatka State University, Kirov 610000, Russia; Institute of Solid-State Chemistry and Mechanochemistry SB RAS, Novosibirsk, 630090, Russia; ORCID 0000-0002-0700-662X; a.v.kuzmin@yandex.ru

Conflict of interest: the authors declare no conflict of interest.